Matter and Radiation at Extremes | RESEARCH ARTICLE | scitation.org/journal/mre

# A molecular dynamics study of laser-excited gold

Cite as: Matter Radiat. Extremes 7, 036901 (2022); doi: 10.1063/5.0073217
Submitted: 28 September 2021 • Accepted: 3 March 2022 •
Published Online: 31 March 2022

View Online Export Citation CrossMark

Jacob M. Molina[a] and T. G. White

## AFFILIATIONS

University of Nevada, Reno, Nevada 89557, USA

[a]Author to whom correspondence should be addressed: jmmolina@nevada.unr.edu

## ABSTRACT

The structural evolution of laser-excited systems of gold has previously been measured through ultrafast MeV electron diffraction. However, there has been a long-standing inability of atomistic simulations to provide a consistent picture of the melting process, leading to large discrepancies between the predicted threshold energy density for complete melting, as well as the transition between heterogeneous and homogeneous melting. We make use of two-temperature classical molecular dynamics simulations utilizing three highly successful interatomic potentials and reproduce electron diffraction data presented by Mo *et al.* [Science **360**, 1451–1455 (2018)]. We recreate the experimental electron diffraction data, employing both a constant and temperature-dependent electron–ion equilibration rate. In all cases, we are able to match time-resolved electron diffraction data, and find consistency between atomistic simulations and experiments, only by allowing laser energy to be transported away from the interaction region. This additional energy-loss pathway, which scales strongly with laser fluence, we attribute to hot electrons leaving the target on a timescale commensurate with melting.



## I. INTRODUCTION

Ultrafast laser excitation of a metal is able to bring the material into a state far from equilibrium.[1,2] The preferential and rapid heating of one subsystem over the other leads to a system of highly coupled cold ions immersed in a partially degenerate electron sea.[3] These transient states commonly occur during the formation of high energy density plasmas, including warm dense matter (WDM), with particular relevance to laser micromachining[4–7] and inertial confinement fusion experiments.[8] In the laboratory, these transient states serve as a testbed where quantum mechanical theories of electron–ion interactions, nuclear dynamics, and phase transitions can be validated.[9–12]

Historically, the response of the electron subsystem has been measured in optical pump–probe experiments.[13–17] However, these model-dependent techniques provided only a surface measurement of the electron properties and limited information on the ionic response. More recently, x-ray scattering experiments have measured the bulk electron temperature by observing the electron plasmon feature.[18] By contrast, the bulk ion temperature has only been inferred from the atomic structure, measured through ultrafast electron[10] or x-ray diffraction.[19,20] When the ionic system is still crystalline, the Debye–Waller factor (i.e., the reduction in the intensity of the Laue diffraction peaks) is a practical, albeit model-dependent, method.[19,20] However, modeling the decay of the Laue diffraction peak, which is ultimately dependent on the root-mean-square (rms) deviation of the atoms from their lattice positions, depends on several physical parameters:

- the energy density of the sample $\varepsilon$,
- the electron–ion equilibration rate $g_{ei}(T_e, T_i)$,
- the electronic heat capacity $C_e(T_e)$,
- the ionic heat capacity $C_i(T_i)$,
- the Debye temperature $T_D(T_e, T_i)$,

where the generally assumed dependences on electron temperature $T_e$ and ion temperature $T_i$ are shown. While the electronic and ionic heat capacities are well constrained for gold,[21,22] the values found in the literature for the remaining three parameters exhibit large uncertainties. In particular, theoretical predictions of the equilibration rate vary by up to an order of magnitude.[22–29]

During the last decade, three different experiments have used ultrafast electron diffraction to measure the decay of the Laue diffraction peaks in laser-irradiated gold. They each attempted to elucidate the effects of nonequilibrium species on the interatomic potential. i.e., to measure the nonequilibrium Debye temperature and answer the long-standing question surrounding the existence of bond hardening/softening in warm dense gold.[10–12,30] For comparable fluences, each experiment measured similar decays in the Laue diffraction peaks. However, they reached opposing conclusions; this was primarily due to different assumptions regarding the behavior of the electron–ion equilibration rate and the initial energy density deposited into the sample. For example, Daraszewicz and co-workers found that the assumed initial energy density $\mathscr{E}$, calculated by taking

into consideration purely the reflected and transmitted light, was reduced by a factor of $\eta$:[11]

$$\varepsilon = \eta \mathscr{E}, \tag{1}$$

where $\varepsilon$ is the corrected energy density. They obtained a value of $\eta \sim 0.5$, measured through independent optical absorption methods at lower laser fluences.[31] At higher fluences, they found it necessary to treat $\eta$ as a free parameter. This extra energy-loss pathway, specific to the target and experimental geometry, was attributed to ballistic/fast electron transport away from the system—despite contemporary claims that the value of $\eta$ was negligible.[32]

One method of modeling such experiments is classical molecular dynamics (MD). When coupled to an electronic system through an appropriate thermostat, such simulations can, in one dimension, simulate the full target thickness, thus capturing the necessary strongly coupled nature of the ions.[33] However, recent efforts using the highly optimized and validated interatomic potential developed by Sheng *et al.*[34,35] were unable to reproduce the experimental results for all energy densities in tandem.[36]

In contrast to previous simulation work, we treat both the electron–ion equilibration rate $g_{ei}$ and the initial energy density $\varepsilon$ as free parameters to provide a consistent description of melting in warm dense gold. Initially, we make use of a constant $g_{ei}$ throughout each simulation, as well as exploring three different interatomic potentials. In all cases, we are able to obtain excellent agreement between the decays of Laue diffraction peaks obtained experimentally and those calculated from synthetic diffraction patterns. We find a strongly energy-dependent electron–ion equilibration rate, in addition to considerable differences between the assumed energy density $\mathscr{E}$ and the energy density in the simulations $\varepsilon$. In fact, for each interatomic potential that we have tested, we have found that the success of the model is contingent on allowing energy to escape from the target region. This additional energy loss, which we also characterize by $\eta$, scales strongly with laser intensity. Additionally, we have implemented several published electron-temperature-dependent (ETD) and ion-temperature-dependent $g_{ei}$ models.[21–23,25,26,29] For all forms of $g_{ei}$, consistency between the simulated and measured diffraction patterns is only achieved by reducing the absorbed energy density.

By introducing the free parameter $\eta$, we present a consistent description of the melting process in warm dense gold, resolving long-standing discrepancies between MD simulations and experiments. Our finding of a non-negligible $\eta$ parameter is in good agreement with the work of Daraszewicz and co-workers; however, we additionally observe a strong dependence on laser intensity.

## II. COMPUTATIONAL METHODS

We perform large-scale MD simulations in the Large-scale Atomic/Molecular Massively Parallel Simulator (LAMMPS) software package[37] in the canonical ensemble. The ions, treated explicitly, are coupled to an electron subsystem through a Langevin thermostat within the two-temperature model (TTM).[38,39] Justified by the rapid electron thermalization time,[40] we heat the electrons instantaneously to simulate the laser–matter interaction; we verify the accuracy of this procedure in the supplementary material by comparing the results of the forthcoming analysis with simulations taking the temporal width of the laser pulse into account. Synthetic diffraction patterns are produced for comparison with the experimental electron diffraction data of Mo *et al.*[10]

In this work, we focus on benchmarking the data obtained by Mo *et al.*, which is expected to be below the threshold for considerable changes in interatomic bond strength.[10,11] In keeping with the experimental conditions, we model free-standing 35 nm single-crystalline gold films and compare our Laue peak decay with measured results for the three assumed energy densities $\mathscr{E}$ = 0.18, 0.36, and 1.17 MJ/kg, referred to here as the low, intermediate, and high energy density cases.

We model the nonequilibrium conditions of the laser-irradiated system via a traditional TTM that describes the evolution of the electron temperature through

$$C_e(T_e)\frac{\partial T_e}{\partial t} = -g_{ei}(T_e - T_i), \tag{2}$$

where $C_e(T_e)$ is the temperature-dependent electron heat capacity. All simulations utilize an electronic heat capacity derived from *ab initio* simulations[21] and found to be in good agreement with previous thermal conductivity experiments.[17] Within each simulation, the electron–ion equilibration rate is treated as a constant, and we employ a 1 fs time step throughout. In addition, before coupling the two subsystems, we equilibrate just the ions for 6.5 ps using a velocity-scaling thermostat and Berendsen barostat[41] in order to bring the system to a temperature of 300 K at atmospheric pressure. This introduces an initial energy density into the ionic subsystem of ~0.05 MJ/kg.

The ballistic electrons, accelerated by the optical laser, have a mean free path of ~100 nm, approximately three times the thickness of the foil, and therefore we approximate the heating as isochoric.[13,42–44] The high thermal conductivity[45] also allows us to retain a single spatially invariant electron temperature and thus avoid complications due to lattice expansion.[36] This is particularly important to avoid spurious edge effects, which may initiate heterogeneous melting. For the duration of the simulation, to model the electron–ion energy exchange, we couple the ions to this single-temperature electron bath via a Langevin thermostat given by[46,47]

$$m\frac{\partial \mathbf{v}_i}{\partial t} = \mathbf{F}_i - \gamma \mathbf{v}_i + \mathbf{f}_L(T_t), \tag{3}$$

where $\mathbf{v}_i$ is the velocity of ion $i$, $\mathbf{F}_i$ is the force acting on ion $i$ due to its interaction with the surrounding atoms at time $t$, $m$ is the ion mass, and $\gamma$ is the friction parameter that characterizes the electron–ion equilibration rate. The friction parameter is related to the equilibration rate through $\gamma = g_{ei}m/3nk_B$, where $n$ is the ion number density and $k_B$ is Boltzmann's constant.[38,39] The $\mathbf{f}_L(T_t)$ term is a stochastic force term with a Gaussian distribution and a mean and variance given by[38,48]

$$\langle \mathbf{f}_L(T_t) \rangle = 0, \tag{4}$$

$$\langle \mathbf{f}_L(T_t) \cdot \mathbf{f}_L(T_{t'}) \rangle = 2\gamma k_B T_e \delta(t - t'). \tag{5}$$

We utilize the highly optimized embedded atom method (EAM) interatomic potential developed by Sheng *et al.*[34] Under equilibrium conditions, the properties of this potential are closely matched with experimental values, as shown in Table I. Additionally, as demonstrated in Fig. 1, the atomic rms deviation and corresponding Debye temperature, obtained in x-ray diffraction experiments, are well

**TABLE I.** Experimentally measured properties of face-centered cubic (fcc) gold alongside those reproduced in molecular dynamics simulations using the interatomic potentials developed by Sheng *et al.* and the electron-temperature-dependent (ETD) potential of Norman *et al.* Here, the values shown for the Norman *et al.* potential are for the variant of the potential calculated for $T_e \sim 0.1$ eV.

| Property | Sheng *et al.*[34] | Norman *et al.*[49] | Experiment |
|---|---|---|---|
| Melt temperature (K) | 1320 | 1208 | 1337 (Ref. 50) |
| Lattice constant (Å) | 4.078 | 4.155 | 4.078 (Ref. 51) |
| Liquid density (g/cm$^3$) | 17.10 | 17.70 | 17.10 (Ref. 52) |
| Melting enthalpy (kJ/mol) | 11.10 | | 12.80 (Ref. 53) |

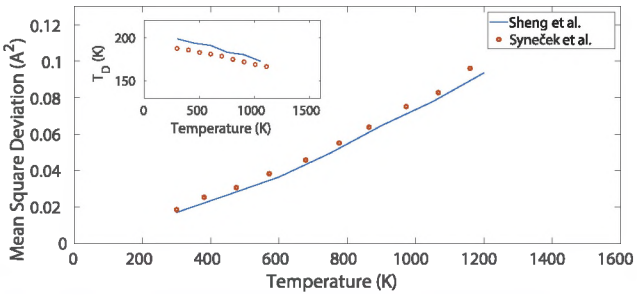


**FIG. 1.** Comparison of the atomic mean square deviation and Debye temperature, $T_D$, produced by interatomic potential developed by Sheng *et al.*[32] and the values obtained from x-ray diffraction measurements at equilibrium temperatures up to melting by Syneček *et al.*[54]

matched at equilibrium temperatures up to melting. In nonequilibrium matter, the Sheng *et al.* potential has been able to successfully match experimental lattice disassembly times after laser irradiation.[34,35]

We utilize two simulation geometries: either a parallelepiped of $(86a_0 \times 15a_0 \times 15a_0)$ or one of $(86a_0 \times 70a_0 \times 70a_0)$, where $a_0 = 4.078$ Å is the lattice constant of gold predicted by the Sheng *et al.* potential. The smaller volume contains 77 400 atoms and the larger volume 1 685 600 atoms. In the larger direction, which corresponds to the 35 nm thickness of the gold foils used in the experiment, the simulation box is much larger than the size of the target geometry, creating front and rear surfaces capable of expansion. In the two smaller directions, we adopt periodic boundary conditions. The smaller geometry is employed when calculating the decay of the Laue peaks. The larger volume, which produces the same Laue decay curve as the smaller volume, allows for a higher resolution in reciprocal space and is used to create the synthetic spatially dependent diffraction patterns out to 50 ps.

## III. MATCHING EXPERIMENTAL DATA

We use the decay of the (220) and (420) Laue diffraction peaks as a metric to compare the simulation and experiment. We obtain the intensity of the diffraction peaks from the static structure factor of the system, which is easily calculated from the Fourier transform of the atomic positions.[55,56] For 3.2 MeV electrons, whose wave vector ($\sim 2 \times 10^{13}$ rad/m) is orders of magnitude higher than their scattering vector ($\sim 10^{10}$ rad/m), the Ewald sphere can be considered flat over a finite region of reciprocal space. As such, we take a $Q_x$–$Q_y$ slice of reciprocal space, where the $x$ and $y$ coordinates run parallel to the surface of the foil. The scattering intensity is calculated by integrating over a specific reflection.

In finding the best fits for all three experimental datasets, we have performed hundreds of simulations utilizing the small simulation geometry. We have considered initial electron temperatures $T_e^0$ that, when converted into energy densities via the electron heat capacity,[21] correspond to a range in $\eta$ of $0 \le \eta \le 1$, with a step size $\Delta T_e^0 = 100$ K. We have considered values of $g_{ei}$ in the range of $0 \le g_{ei} \le 20 \times 10^{16}$ W m$^{-3}$ K$^{-1}$, with a step size of approximately $\Delta g_{ei} \sim 0.3 \times 10^{16}$ W m$^{-3}$ K$^{-1}$. We quantify the best fit by identifying which $(T_e^0, g_{ei})$ pair minimizes the rms difference between the experimental and calculated decays in the intensity of the (220) and (420) Laue diffraction peaks. For each of the three energy densities investigated, this difference is shown in Figs. 2(a)–2(c), with the corresponding best decay curve and temperature evolution for the subsystems given in Figs. 2(d)–2(i). The black dashed line in Figs. 2(a)–2(c) encloses the region in which the simulation results lie within the experimental error bars. In each case, we are able to find a $(T_e^0, g_{ei})$ pair that gives excellent agreement with the experimentally measured decay curves.

For the low energy density case, we find that values of $T_e^0 = 7800 \pm 300$ K and $g_{ei} = 2.2 \pm 0.5 \times 10^{16}$ W m$^{-3}$ K$^{-1}$ produce the best fit. The obtained value of $g_{ei}$ is in good agreement with experimental measurements of $g_{ei}$ in room temperature gold.[13,57] The initial electron temperature corresponds to a corrected energy density in the electron subsystem of $\varepsilon \sim 0.17 \pm 0.01$ MJ/kg, corresponding to $\eta \sim 0.92$. In the intermediate energy density case, we find that $T_e^0 = 8500 \pm 300$ K and $g_{ei} = 5.0 \pm 0.5 \times 10^{16}$ W m$^{-3}$ K$^{-1}$ produce the best fit, corresponding to a corrected initial energy density for the electron subsystem of $\varepsilon \sim 0.21 \pm 0.01$ MJ/kg, with $\eta \sim 0.57$. Finally, in the high energy density case, we find that the best fit to experimental data comes from values of $T_e^0 = 9900 \pm 300$ K and $g_{ei} = 15.0 \pm 2.0 \times 10^{16}$ W m$^{-3}$ K$^{-1}$, corresponding to a corrected initial energy density for the electron subsystem of $\varepsilon \sim 0.3 \pm 0.01$ MJ/kg, and thus $\eta \sim 0.26$. Our analysis demonstrates a strong dependence of the parameter $\eta$ and the electron–ion equilibration rate on the assumed energy density, i.e., the energy density calculated by taking into consideration purely the reflected and transmitted light (cf. the dashed black lines in Fig. 3).

The bond strength in nonequilibrium gold is predicted to change when the electron temperature is significantly higher than the ion temperature. We check the effect of this on our conclusions by repeating the analysis with two additional interatomic potentials designed to take into account higher temperature electrons,[49] both of which are validated against finite temperature Kohn–Sham density functional theory.[58] The first, shown by the dashed blue lines

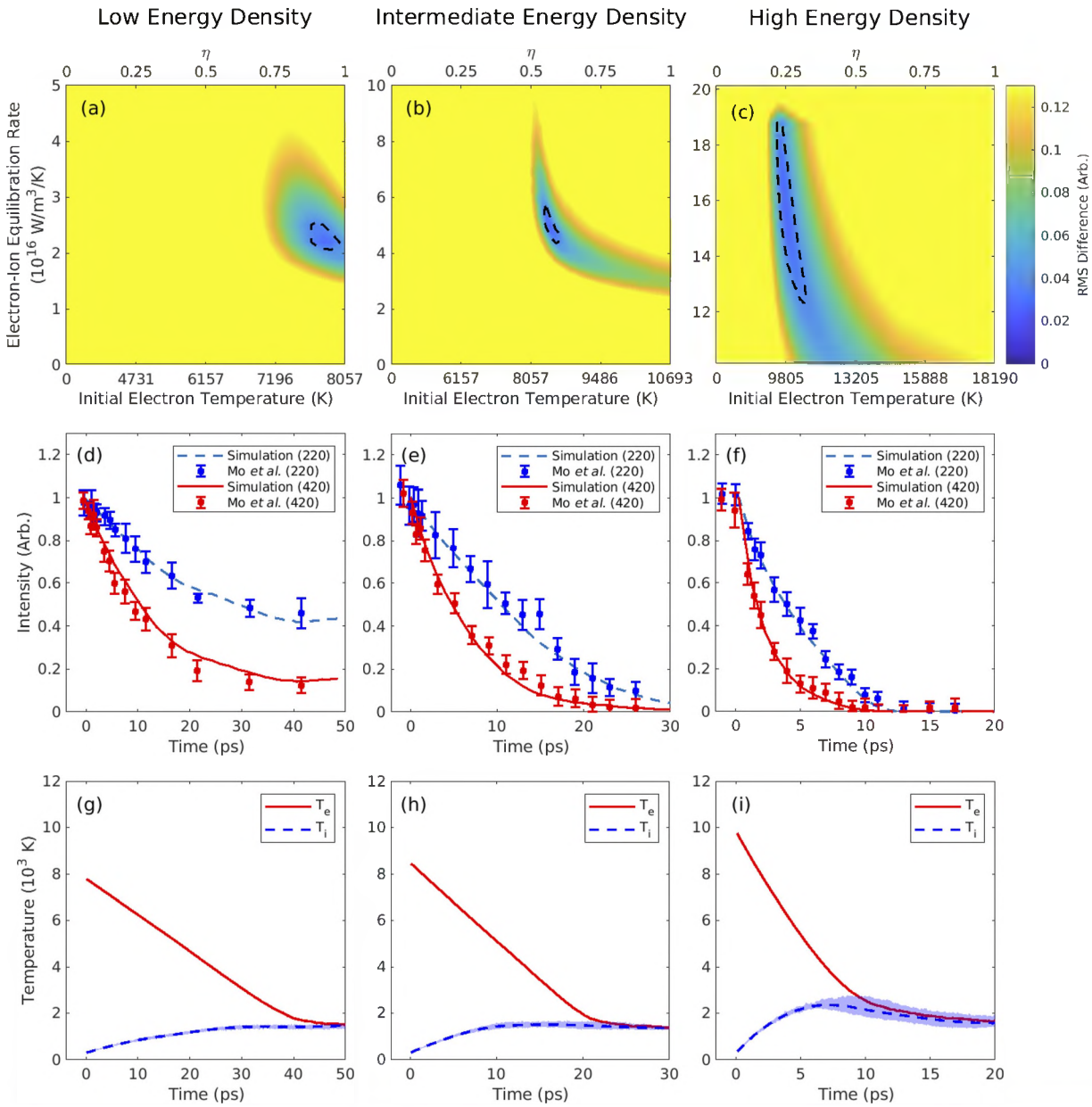


**FIG. 2.** Comparison between experimentally obtained Laue decay curves[10] and those given by molecular dynamics simulations. (a)–(c) The rms difference between simulated and experimental decay curves for a range of initial electron temperatures and electron–ion equilibration rates. Here, the rms differences of the (220) and (420) curves have been added in quadrature. The area enclosed by the dashed line encompasses the region in which the simulation results lie within the experimental error bars. (d)–(f) Comparisons, for each energy density, of the experimental and simulated decays of the (220) and (420) Laue peaks for best-fit values of $T_e^0$ and $g_{ei}$ obtained in (a)–(c). (g)–(i) The corresponding temporal evolutions of the electron and ion temperatures. Here, the area shaded in blue represents the variation in the ion temperature across the sample.

in Fig. 3, is calculated for electrons at a temperature of 0.1 eV (~1200 K) and found to be in close agreement with those produced by the interatomic potential developed by Sheng *et al.* (a comparison of the properties of these two interatomic potentials can be found in Table I). Here, we find there to be a ~11% difference between the best-fit results produced by the potential developed by Sheng *et al.* and that developed by Norman *et al.*[34,49] For the second potential, calculated for an electron temperature of 1.5 eV (~17 400 K), we only consider results in the high energy density case. Here, we find $\eta = 0.15$, which is less than that in the case of the Sheng potential, corresponding to an even more substantial reduction in absorbed energy (cf. the square red points in Fig. 3). Figures S1 and S2 in the supplementary material depict the full results of this analysis.

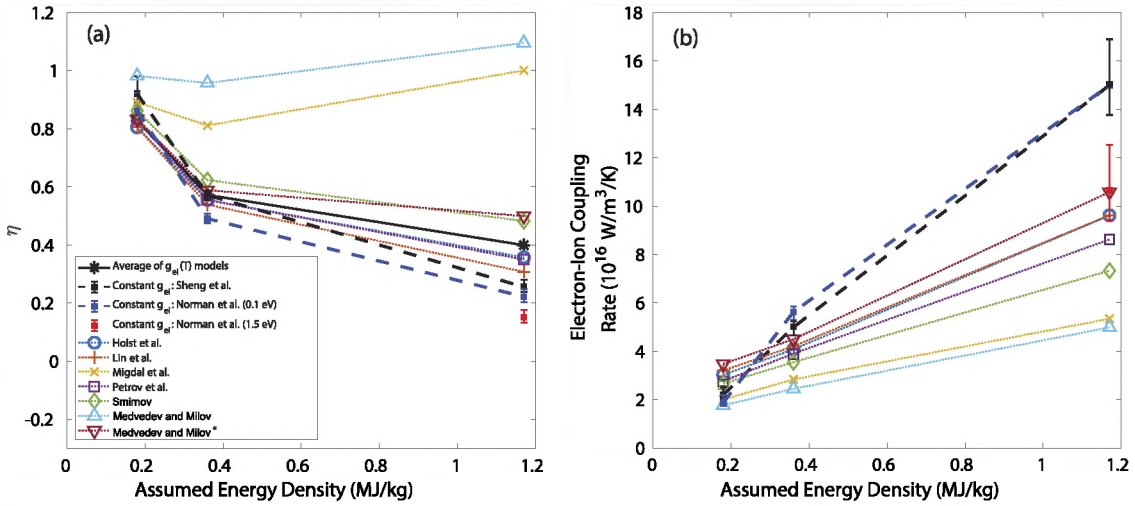


**FIG. 3.** (a) Evolution of best-fit values of $\eta$ for several functional forms of the electron–ion equilibration rate.[21–23,25,26,29] Here, Medvedev *et al.** is used to denote the $g_{ei}(T_e, T_i)$ prediction that is both electron- and ion-temperature-dependent. In our calculations of the average $\eta$ for all theoretical models, we exclude the outlier results produced by the solely electron-temperature-dependent model calculated by Medvedev and Milov at a constant ion temperature of 300 K, and the Migdal *et al.* model. (b) Average value of $g_{ei}$ for a given energy density up until melting. The value plotted has been calculated by taking the average over the $g_{ei}$ value present out until 50, 25, and 10 ps in the low, intermediate, and high energy density cases, respectively.

We find, across multiple potentials, an $\eta$ parameter between 0.2 and 1 that scales strongly with the assumed energy density. Our result agrees qualitatively with previous work, which measured a value of 0.5 for similar conditions.[11] In that work, it was suggested that the origin of the lost energy is energy dissipation into the supporting grid by ballistic electrons or electron ejection from the rear of the target.[11] Other studies have suggested that the temporary formation of an electron sheath around the surface of the target[59] accounts for a decrease in the energy

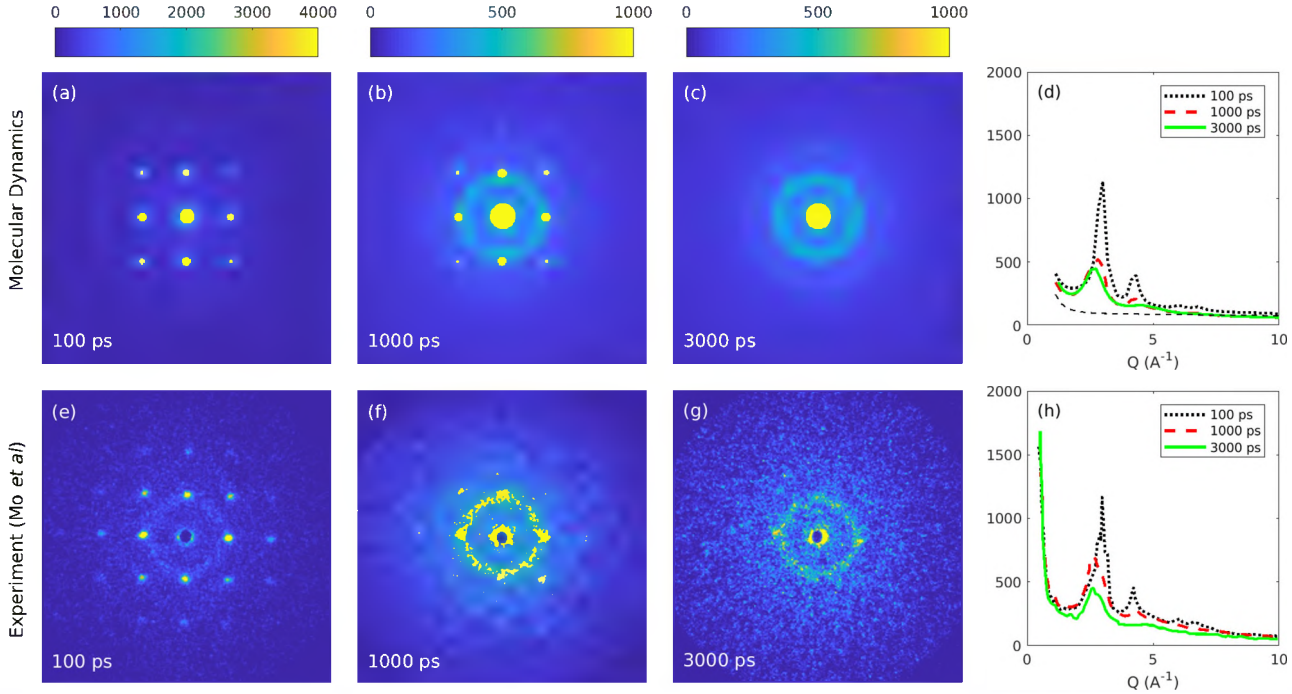


**FIG. 4.** Comparison of simulated and measured spatially resolved diffraction pattern data for the low energy density case. (a)–(c) Spatially resolved data from the simulation for 100, 1000, and 3000 ps. (d) Angularly resolved diffraction data obtained from azimuthal integrals of the data shown in (a)–(c). (e)–(g) Spatially resolved data obtained by Mo *et al.*[10] (h) Angularly resolved diffraction data obtained from azimuthal integrals of the data shown in (e)–(g).

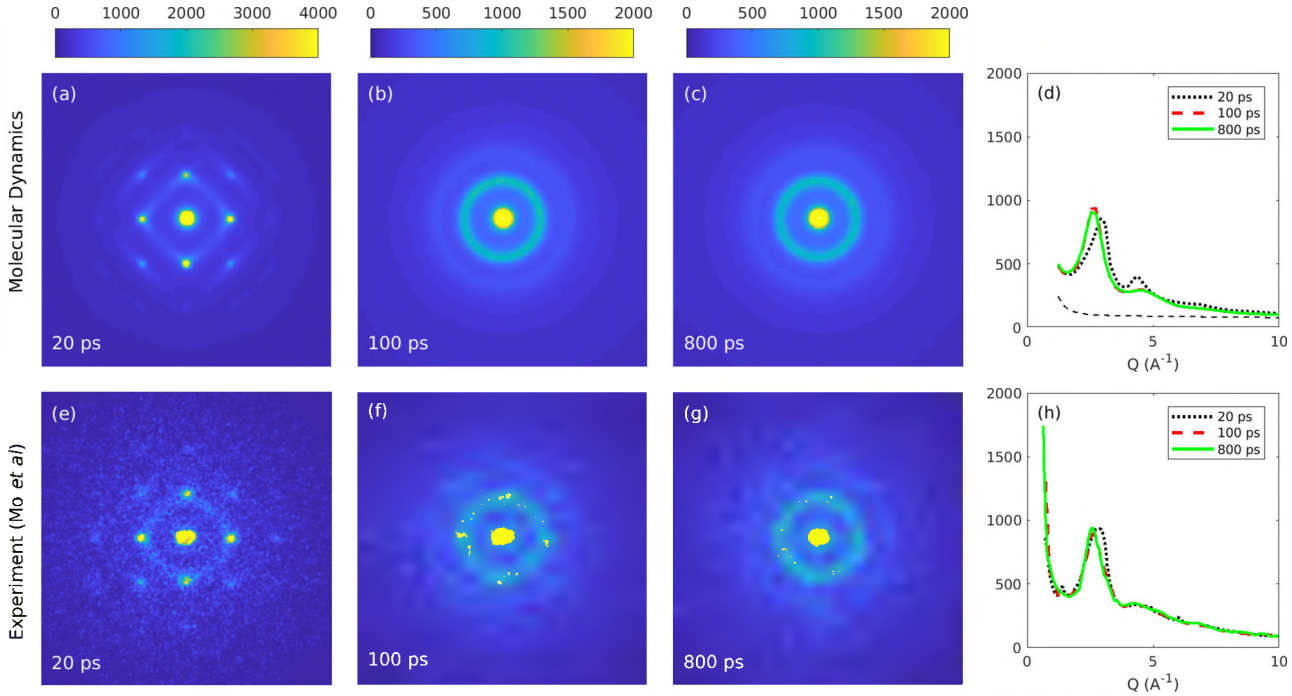


**FIG. 5.** Same as Fig. 4, but for the intermediate energy density case and times of 20, 100, and 800 ps.

density on a timescale commensurate with the decay of the Laue peaks.[60,61] Our scaling with the assumed energy density, which is proportional to the laser fluence for constant target thickness, corroborates this conclusion. We note that this interpretation makes the $\eta$ parameter specific to the target and experimental geometry and thus complicates the interpretation of such experiments.

### A. Spatially resolved diffraction patterns

For each of the three energy density cases, we take the best simulation achieved with a constant $g_{ei}$, and predict spatially resolved synthetic diffraction patterns. For the first 50 ps, these are created by Fourier transforming the atomic positions taken from simulations using the larger geometry and taking a $Q_x$–$Q_y$ slice of reciprocal space. In each case, we confirm that these larger simulations reproduce the Laue peak decay seen in the smaller simulations. The diffraction patterns, shown in Figs. 4–6, correspond to the three energy density cases. The timescales of the experimental diffraction pattern measurements necessitate the use of the smaller simulation geometry in producing Figs. 4–6 for times above 50 ps. Also shown, for comparison, are the experimentally obtained diffraction patterns.

For a direct comparison with the measured spatially resolved electron scattering data of Mo *et al.*, the simulated structure factor is multiplied by the electron scattering form factor, which is calculated using the Mott–Bethe formula[62] utilizing tabulated x-ray elastic scattering cross-sections.[63] Above ~2 Å$^{-1}$, we find a negligible difference between the use of a cold or singularly ionized form factor. In addition, a background term of the form[64,65]

$$\frac{d\sigma_{inel}}{d\Omega} = \frac{A}{Q^4}\left[1 - \frac{1}{(1 + B\,Q^2)^2}\right] + mQ + c \tag{6}$$

is introduced to account for inelastic scattering. The coefficients $A = 350$ and $B = 1.3$ are kept constant for all comparisons, whereas small variations are required in the linear component between shots at different laser intensities. In each case, the background term is plotted as a dashed line in the figures and represents a small component of the overall signal. Finally, the entire image is convoluted with a pseudo-Voigt profile that represents the spatial profile of the electron beam[66] ($\mathrm{FWHM_{Gauss}} = 17$ meV and $\mathrm{FWHM_{Lorentz}} = 6.5$ meV).

Initially, we find that the diffraction peaks from the solid gold are an order of magnitude larger than the liquid scattering signal, an effect not seen in the experimental data, where the difference is closer to a factor of two. We attribute this discrepancy to misalignment and beam divergence in the experiment that is not present in the simulations. Therefore, we average over a small $\Delta Q_z$, reducing the intensity of the solid diffraction peaks while leaving the liquid diffraction peaks, which are broad in reciprocal space, unchanged. We choose $\Delta Q_z$, which remains constant in our modeling, by matching the spatially resolved scattering signal at both early ($t = 0$ ps) and late ($t = 17$ ps) times in the high energy density case. With these changes, we are able to match, in each of the three energy density cases, the angularly resolved line-outs obtained in the experiment. It is important to note that the applied modifications to the raw data, used to obtain the angularly resolved data, affect only the qualitative comparisons provided in Figs. 4–6, and not the intensity decay curves in Fig. 2.

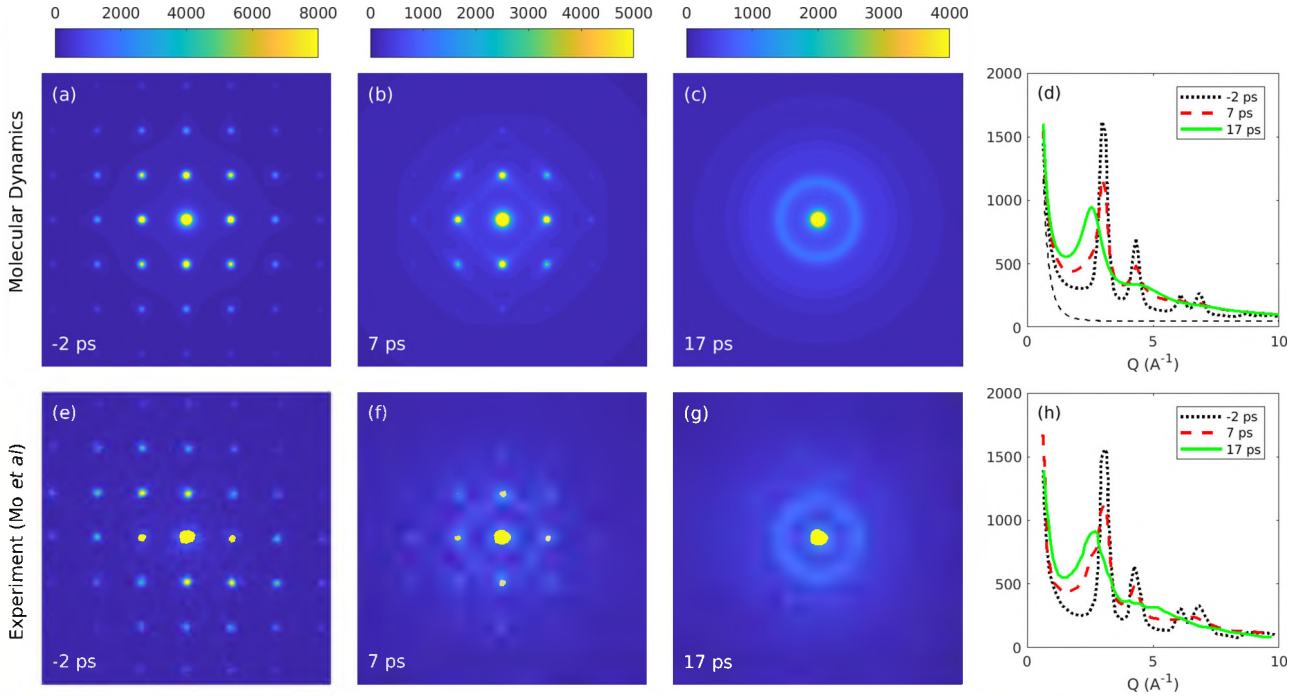


**FIG. 6.** Same as Fig.4, but for the high-energy density-case and times of −2, 7, and 17 ps.

### B. Heterogeneous/homogeneous melting

In our analysis of the melting behavior of the sample, we utilize the smaller simulation geometry. This is because of a lack of available computational resources that would allow us to perform simulations in the large simulation geometry that capture the full duration of the low and intermediate energy density cases (3000 and 800 ps, respectively). We are however, able to compare the small and large geometries, in all three energy density cases, out to 50 ps. In all energy density cases, we find the melting behavior and the expansion rates of the large and small geometry samples to be equivalent out to 50 ps.

From the time for the total disappearance of the (200) peak, Mo *et al.*[10] concluded that the three energy density cases correspond to the incomplete, heterogeneous, and homogeneous melting processes, respectively. On this basis, they obtained a threshold for complete melting (assuming total absorption of the laser energy, $\eta = 1$) of ~0.25 MJ/kg and a transition between heterogeneous and homogeneous melting of ~0.38 MJ/kg. Of note, both of these values are higher than those predicted by molecular dynamics simulations employing the interatomic potential of Zhou *et al.*[67,68]

In our analysis, utilizing the interatomic potential developed by Sheng *et al.*,[34] we are able to match the entire decay of the experimentally measured Laue peak. Using the OVITO visualization tool[69] together with polyhedral template matching,[70] we can directly assess the structure and melting process in each of our cases (cf. Fig. 7). In contrast to the original work, we find that the low energy density case exhibits heterogeneous melting, with a clear propagation of the melt front [see Figs. 7(a)–7(c)] and no nucleation of melt inside the target. The two higher energy densities both exhibit homogeneous melting, with the intermediate case appearing to be on the cusp of the two regimes, as determined from nonuniform melt regions inside the target. Taking this into consideration, and the lower predicted energy density from the $\eta$ parameter, we find a total energy density threshold for complete melting below 0.22 MJ/kg (which includes the 0.17 MJ/kg present in the electron subsystem and the 0.05 MJ/kg already present in our 300 K gold sample). This value is in agreement with the expected value of 0.22 MJ/kg.[71] For the transition between homogeneous and heterogeneous melting, we find a value that lies between 0.22 and 0.26 MJ/kg. With the introduction of the $\eta$ parameter, we find that the complete melting threshold, and heterogeneous-to-homogeneous melting boundaries, are both lower than previously thought.[10]

Finally, we note that despite achieving excellent agreement with the experimental decay curves, we are not able to reproduce the low intensity, long lived, diffraction features present in the experiment [cf. Figs. 5(b) and 5(f)]. We find that the intermediate energy density case melts within 100 ps, whereas the original work concludes that it does not melt until 800 ps. To investigate if this is a fault of the equilibration rate, we manually adjust the value of $g_{ei}$ throughout the simulation to best match the experimental results; we are unable to match both the early-time Laue peak decay and late time long lived diffraction patterns. In the simulation, this may highlight a deficiency in either the TTM model or the interatomic potential. In the experiment, this could be attributed to inhomogeneous heating.

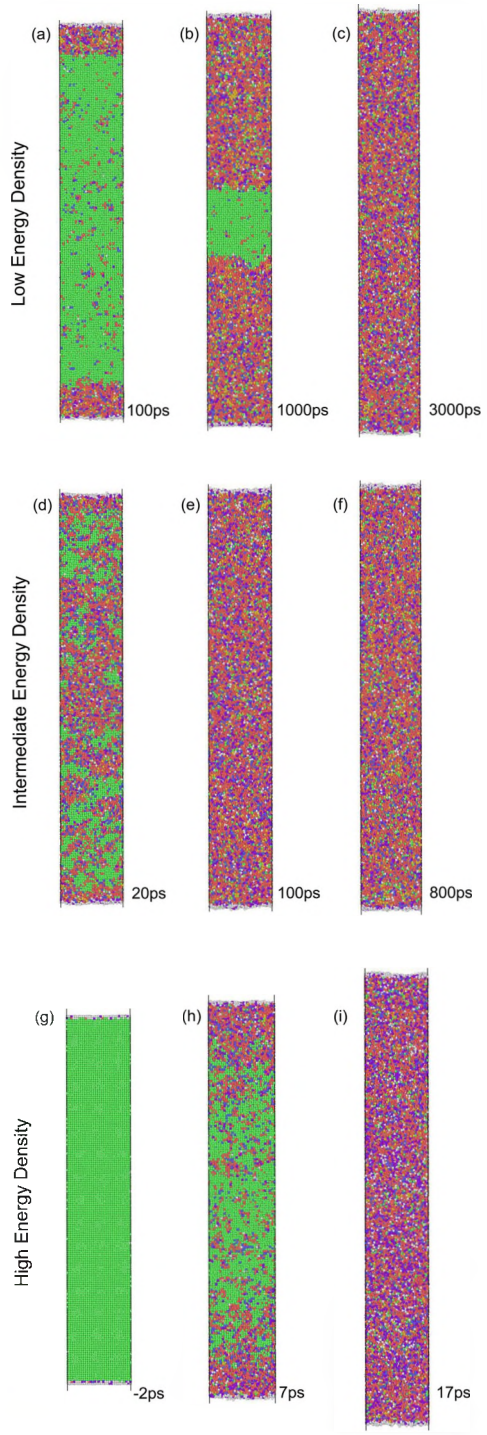


**FIG. 7.** Visualization of gold melting in the low [(a)–(c)], intermediate [(d)–(f)], and high [(g)–(i)] energy density cases via the technique of polyhedral template matching[70] in OVITO visualization software.[69] For each energy density case, the time steps corresponding to the diffraction patterns shown in Figs. 4–6 are presented. The green color identifies the fcc lattice type, whereas the non-green colors identify liquid present in the sample. These results were produced using the smaller simulation geometry.

## IV. TEMPERATURE-DEPENDENT ELECTRON–ION EQUILIBRATION RATES

The electron–ion equilibration rate $g_{ei}$ is predicted to scale strongly with both electron and ion temperature. Thus, to supplement our study, we employ seven models of temperature-dependent equilibration rates.[21–23,25,26,29] This set of simulations is performed

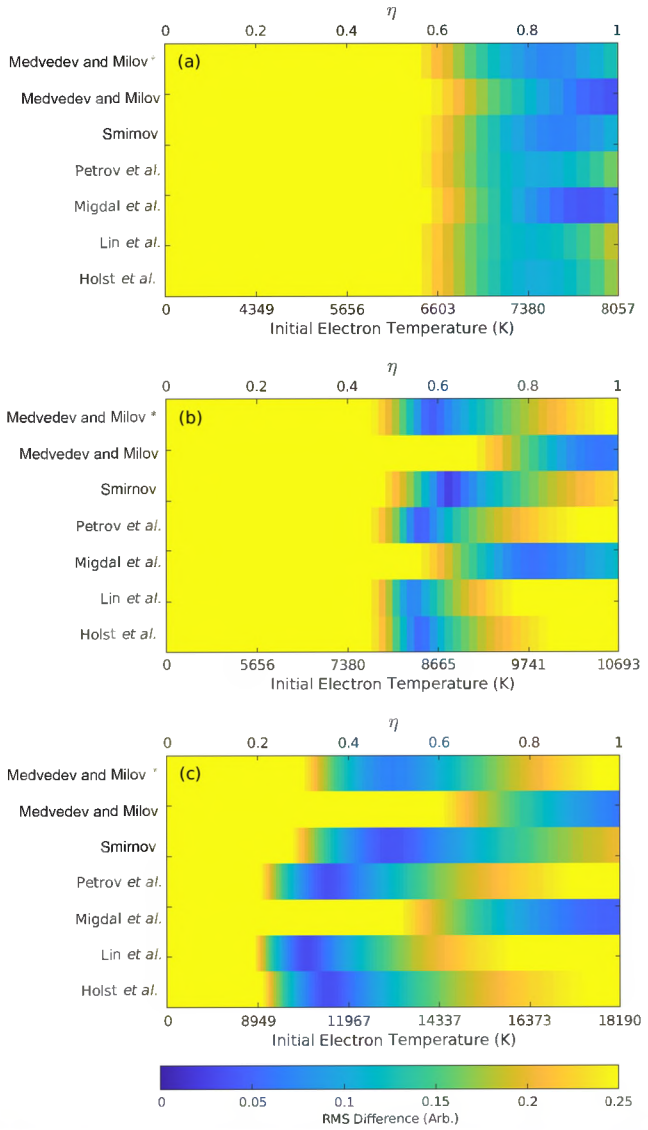


**FIG. 8.** Comparison between experimentally obtained Laue decay curves[10] and those given by molecular dynamics simulations utilizing temperature-dependent electron–ion equilibration rates[21–23,25,26,29] for the low (a), intermediate (b), and high (c) energy density cases. Here, "Medvedev *et al.**" is used to denote a $g_{ei}(T)$ prediction that is both electron- and ion-temperature-dependent.[23] For all three energy density cases, the rms difference between simulated and experimental decay curves for a range of initial electron temperatures is shown for each of the employed $g_{ei}(T)$ models. In our analysis, the rms differences of the (220) and (420) curves have been added in quadrature.

under the same specifications outlined in Sec. II and use the smaller simulation geometry. As in Sec. III, we use the decay of the (220) and (420) Laue diffraction peaks to draw comparisons between simulation and the experimental results obtained by Mo *et al.*[10] In each energy density case, we consider only a temperature range corresponding to $\eta$ in the range $\sim 0 \leq \eta \leq 1$, so as to consider only physically possible values. The performance of each model can be seen in Fig. 8. In the low energy density case, shown in Fig. 8(a), we find that the Medvedev and Milov[23] model, calculated for a constant ion temperature of 300 K, and the Migdal *et al.*[26] model perform best. For the intermediate energy density case, shown in Fig. 8(b), we find that the model developed by Smirnov[25] has the lowest rms difference. Finally, in the high energy density case, shown in Fig. 8(c), we find that the models developed by Lin *et al.*,[22] Holst *et al.*,[21] and Petrov *et al.*[29] perform best. Considering all three energy density cases simultaneously, the model developed by Smirnov[25] performs best.

The success of these theoretical models is contingent on a similar inclusion of energy loss as was found in the constant-$g_{ei}$ description. Using the best-fit value of $T_e^0$, we can calculate the $\eta$ parameter for each theoretical model and each energy density case. The evolution of the $\eta$ factor for both the constant-$g_{ei}$ case and the temperature-dependent $g_{ei}$ models is shown in Fig. 3(a). The electron-temperature-dependent models display a similar trend in $\eta$ as the constant case, except for the solely electron-temperature-dependent model developed by Medvedev and Milov,[23] calculated for a constant ion temperature of 300 K, and the model developed by Migdal *et al.*[26] Excluding these outliers on the basis that they predict either energy gain or no energy loss in the system, we calculate the average $\eta$ across all of our tested models. We find values of $\eta \sim 0.83$, 0.57, and 0.40 for the low, intermediate, and high energy density cases respectively, which are very close to that for the constant-$g_{ei}$ case.

In Fig. 3(b), as a method of comparing models of $g_{ei}$ with different functional dependences, we plot the average value of $g_{ei}$ in the best-fit simulation for each theoretical model, as well as the constant-$g_{ei}$ cases discussed in Sec. III. In each simulation, we average the value of $g_{ei}$ out until the time at which the decrease in the Laue decay curves stops; in the low, intermediate, and high energy density cases, these times correspond to 50, 25, and 10 ps, respectively. In Figs. 3(a) and 3(b), the best-fit results for the constant and temperature-dependent $g_{ei}$ models are in close agreement with one another for the low and intermediate energy density cases. However, they diverge in the high energy density case. This discrepancy could be due to bond softening, which is predicted to occur in gold, at its equilibrium volume, for electron temperatures $T_e > 9000$ K (or an energy density of ~0.24 MJ/kg).[11] Our results suggest that in the high energy density case, the initial electron temperature of the sample is expected to be above $T_e^0 \sim 9000$ K.

## V. CONCLUSION

We have benchmarked the molecular dynamics simulations of the ultrafast excitation of thin gold films against experimental MeV electron diffraction results published by Mo *et al.*[10] We have carried out this analysis using a constant electron–ion coupling rate, seven prominent temperature-dependent electron–ion coupling rate models, and three different interatomic potentials. Using the Laue peak decay as a metric, and treating the initial energy density and the electron–ion equilibration rate as free parameters, we have found a strong dependence of the $\eta$ parameter on initial energy density, with increased energy loss at higher energy densities (and higher laser fluence), which is in good agreement with the work of Daraszewicz *et al.*[11] We believe the need for an additional energy loss pathway, and the presented scaling with increased fluence, to be reliably established. Ultimately, this ambiguity needs to be resolved via direct measurement of the subsystem temperatures.

## SUPPLEMENTARY MATERIAL

See the supplementary material for a discussion of the simulation results utilizing high-temperature potentials, as well as the results depicting the effects of including the temporal width of the laser pulse in our simulations.

## ACKNOWLEDGMENTS

The authors acknowledge M. Z. Mo for providing the experimental data that were used throughout this work. This work was funded in part by the U.S. Department of Energy, National Nuclear Security Administration (NNSA) (Award No. DE-NA0004039). This material is based upon work supported by the National Science Foundation under Grant No. 2045718. The authors acknowledge the support of Research & Innovation and the Office of Information Technology at the University of Nevada, Reno for computing time on the Pronghorn High Performance Computing Cluster. J.M.M. acknowledges funding and support from the Nevada NSF-EPSCoR NEXUS Award and the McNair Scholars Program at the University of Nevada, Reno.

## AUTHOR DECLARATIONS

### Conflict of Interest

The authors have no conflicts to disclose.

## DATA AVAILABILITY

The data that support the findings of this study are available from the corresponding author upon reasonable request.

## REFERENCES

[1]K. H. Bennemann, "Ultrafast dynamics in solids," J. Phys.: Condens. Matter **16**, R995 (2004).
[2]E. G. Gamaly, "The physics of ultra-short laser interaction with solids at non-relativistic intensities," Phys. Rep. **508**, 91–243 (2011).
[3]S. Ichimaru, *Statistical Plasma Physics, Volume II: Condensed Plasmas* (CRC Press, Boca Raton, FL, 2004).
[4]B. H. Christensen, K. Vestentoft, and P. Balling, "Short-pulse ablation rates and the two-temperature model," Appl. Surf. Sci. **253**, 6347–6352 (2007).
[5]K. Sugioka and Y. Cheng, "Ultrafast lasers—Reliable tools for advanced materials processing," Light: Sci. Appl. **3**, e149 (2014).
[6]X. He, A. Datta, W. Nam, L. M. Traverso, and X. Xu, "Sub-diffraction limited writing based on laser induced periodic surface structures (LIPSS)," Sci. Rep. **6**, 35035 (2016).
[7]R. R. Gattass and E. Mazur, "Femtosecond laser micromachining in transparent materials," Nat. Photonics **2**, 219–225 (2008).
[8]S. H. Glenzer, B. J. MacGowan, P. Michel, N. B. Meezan, L. J. Suter, S. N. Dixit, J. L. Kline, G. A. Kyrala, D. K. Bradley, D. A. Callahan, E. L. Dewald, L. Divol, E. Dzenitis, M. J. Edwards, A. V. Hamza, C. A. Haynam, D. E. Hinkel, D. H. Kalantar, J. D. Kilkenny, O. L. Landen, J. D. Lindl, S. LePape, J. D. Moody, A. Nikroo, T. Parham,

M. B. Schneider, R. P. J. Town, P. Wegner, K. Widmann, P. Whitman, B. K. F. Young, B. Van Wonterghem, L. J. Atherton, and E. I. Moses, "Symmetric inertial confinement fusion implosions at ultra-high laser energies," Science **327**, 1228–1231 (2010).

[9]M. Mo, S. Murphy, Z. Chen, P. Fossati, R. Li, Y. Wang, X. Wang, and S. Glenzer, "Visualization of ultrafast melting initiated from radiation-driven defects in solids," Sci. Adv. **5**, eaaw0392 (2019).

[10]M. Z. Mo, Z. Chen, R. K. Li, M. Dunning, B. B. L. Witte, J. K. Baldwin, L. B. Fletcher, J. B. Kim, A. Ng, R. Redmer, A. H. Reid, P. Shekhar, X. Z. Shen, M. Shen, K. Sokolowski-Tinten, Y. Y. Tsui, Y. Q. Wang, Q. Zheng, X. J. Wang, and S. H. Glenzer, "Heterogeneous to homogeneous melting transition visualized with ultrafast electron diffraction," Science **360**, 1451–1455 (2018).

[11]S. L. Daraszewicz, Y. Giret, N. Naruse, Y. Murooka, J. Yang, D. M. Duffy, A. L. Shluger, and K. Tanimura, "Structural dynamics of laser-irradiated gold nanofilms," Phys. Rev. B **88**, 184101 (2013).

[12]R. Ernstorfer, M. Harb, C. T. Hebeisen, G. Sciaini, T. Dartigalongue, and R. J. D. Miller, "The formation of warm dense matter: Experimental evidence for electronic bond hardening in gold," Science **323**, 1033–1037 (2009).

[13]J. Hohlfeld, J. G. Müller, S.-S. Wellershoff, and E. Matthias, "Time-resolved thermoreflectivity of thin gold films and its dependence on film thickness," Appl. Phys. B **64**, 387–390 (1997).

[14]C. Guo and A. J. Taylor, "Nonthermal component in heat-induced structural deformation and phase transition in gold," Phys. Rev. B **62**, R11921(R) (2000).

[15]B. I. Cho, T. Ogitsu, K. Engelhorn, A. A. Correa, Y. Ping, J. W. Lee, L. J. Bae, D. Prendergast, R. W. Falcone, and P. A. Heimann, "Measurement of electron-ion relaxation in warm dense copper," Sci. Rep. **6**, 18843 (2016).

[16]N. Jourdain, L. Lecherbourg, V. Recoules, P. Renaudin, and F. Dorchies, "Electron-ion thermal equilibration dynamics in femtosecond heated warm dense copper," Phys. Rev. B **97**, 075148 (2018).

[17]Z. Chen, B. Holst, S. E. Kirkwood, V. Sametoglu, M. Reid, Y. Y. Tsui, V. Recoules, and A. Ng, "Evolution of ac conductivity in nonequilibrium warm dense gold," Phys. Rev. Lett. **110**, 135001 (2013).

[18]L. B. Fletcher, H. J. Lee, T. Döppner, E. Galtier, B. Nagler, P. Heimann, C. Fortmann, S. LePape, T. Ma, M. Millot, A. Pak, D. Turnbull, D. A. Chapman, D. O. Gericke, J. Vorberger, T. White, G. Gregori, M. Wei, B. Barbrel, R. W. Falcone, C.-C. Kao, H. Nuhn, J. Welch, U. Zastrau, P. Neumayer, J. B. Hastings, and S. H. Glenzer, "Ultrabright X-ray laser scattering for dynamic warm dense matter physics," Nat. Photonics **9**, 274–279 (2015).

[19]T. G. White, N. J. Hartley, B. Borm, B. J. B. Crowley, J. W. O. Harris, D. C. Hochhaus, T. Kaempfer, K. Li, P. Neumayer, L. K. Pattison, F. Pfeifer, S. Richardson, A. P. L. Robinson, I. Uschmann, and G. Gregori, "Electron-ion equilibration in ultrafast heated graphite," Phys. Rev. Lett. **112**, 145005 (2014).

[20]T. G. White, J. Vorberger, C. R. D. Brown, B. J. B. Crowley, P. Davis, S. H. Glenzer, J. W. O. Harris, D. C. Hochhaus, S. Le Pape, T. Ma, C. D. Murphy, P. Neumayer, L. K. Pattison, S. Richardson, D. O. Gericke, and G. Gregori, "Observation of inhibited electron-ion coupling in strongly heated graphite," Sci. Rep. **2**, 889 (2012).

[21]B. Holst, V. Recoules, S. Mazevet, M. Torrent, A. Ng, Z. Chen, S. E. Kirkwood, V. Sametoglu, M. Reid, and Y. Y. Tsui, "*Ab initio* model of optical properties of two-temperature warm dense matter," Phys. Rev. B **90**, 035121 (2014).

[22]Z. Lin, L. Zhigilei, and V. Celli, "Electron-phonon coupling and electron heat capacity of metals under conditions of strong electron-phonon nonequilibrium," Phys. Rev. B **77**, 075133 (2008).

[23]N. Medvedev and I. Milov, "Electron-phonon coupling in metals at high electronic temperatures," Phys. Rev. B **102**, 064302 (2020).

[24]A. M. Brown, R. Sundararaman, P. Narang, W. A. Goddard III, and H. A. Atwater, "*Ab initio* phonon coupling and optical response of hot electrons in plasmonic metals," Phys. Rev. B **94**, 075120 (2016).

[25]N. A. Smirnov, "Copper, gold, and platinum under femtosecond irradiation: Results of first-principles calculations," Phys. Rev. B **101**, 094103 (2020).

[26]K. P. Migdal, D. K. Il'nitsky, Y. V. Petrov, and N. A. Inogamov, "Equations of state, energy transport and two-temperature hydrodynamic simulations for femtosecond laser irradiated copper and gold," J. Phys.: Conf. Ser. **653**, 012086 (2015).

[27]X. Y. Wang, D. M. Riffe, Y.-S. Lee, and M. C. Downer, "Time-resolved electron-temperature measurement in a highly excited gold target using femtosecond thermionic emission," Phys. Rev. B **50**, 8016 (1994).

[28]D. A. Papaconstantopoulos, *Handbook of the Band Structure of Elemental Solids* (Springer US, Boston, MA, 2015).

[29]Y. V. Petrov, N. A. Inogamov, and K. P. Migdal, "Thermal conductivity and the electron-ion heat transfer coefficient in condensed media with a strongly excited electron subsystem," JETP Lett. **97**, 20–27 (2013).

[30]V. Recoules, J. Clérouin, G. Zérah, P. M. Anglade, and S. Mazevet, "Effect of intense laser irradiation on the lattice stability of semiconductors and metals," Phys. Rev. Lett. **96**, 055503 (2006).

[31]Y. Giret, N. Naruse, S. L. Daraszewicz, Y. Murooka, J. Yang, D. M. Duffy, A. L. Shluger, and K. Tanimura, "Determination of transient atomic structure of laser-excited materials from time-resolved diffraction data," Appl. Phys. Lett. **103**, 253107 (2013).

[32]Z. Chen, V. Sametoglu, Y. Y. Tsui, T. Ao, and A. Ng, "Flux-limited nonequilibrium electron energy transport in warm dense gold," Phys. Rev. Lett. **108**, 165001 (2012).

[33]A. Tamm, M. Caro, A. Caro, G. Samolyuk, M. Klintenberg, and A. A. Correa, "Langevin dynamics with spatial correlations as a model for electron-phonon coupling," Phys. Rev. Lett. **120**, 185501 (2018).

[34]H. W. Sheng, M. J. Kramer, A. Cadien, T. Fujita, and M. W. Chen, "Highly optimized embedded-atom-method potentials for fourteen fcc metals," Phys. Rev. B **83**, 134118 (2011).

[35]Z. Chen, M. Mo, L. Soulard, V. Recoules, P. Hering, Y. Y. Tsui, S. H. Glenzer, and A. Ng, "Interatomic potential in the nonequilibrium warm dense matter regime," Phys. Rev. Lett. **121**, 075002 (2018).

[36]Q. Zeng and J. Dai, "Structural transition dynamics of the formation of warm dense gold: From an atomic scale view," Sci. China: Phys., Mech. Astron. **63**, 263011 (2020).

[37]S. Plimpton, "Fast parallel algorithms for short-range molecular dynamics," J. Comput. Phys. **117**, 1–19 (1995).

[38]A. M. Rutherford and D. M. Duffy, "The effect of electron–ion interactions on radiation damage simulations," J. Phys.: Condens. Matter **19**, 496201 (2007).

[39]D. M. Duffy and A. M. Rutherford, "Including the effects of electronic stopping and electron–ion interactions in radiation damage simulations," J. Phys.: Condens. Matter **19**, 016207 (2006).

[40]Z. Chen, Y. Y. Tsui, M. Z. Mo, R. Fedosejevs, T. Ozaki, V. Recoules, P. A. Sterne, and A. Ng, "Electron kinetics induced by ultrafast photoexcitation of warm dense matter in a 30-nm-thick foil," Phys. Rev. Lett. **127**, 097403 (2021).

[41]H. J. C. Berendsen, J. P. M. Postma, W. F. van Gunsteren, A. DiNola, and J. R. Haak, "Molecular dynamics with coupling to an external bath," J. Chem. Phys. **81**, 3684 (1984).

[42]J. Hohlfeld, S.-S. Wellershoff, J. Güdde, U. Conrad, V. Jähnke, and E. Matthias, "Electron and lattice dynamics following optical excitation of metals," Chem. Phys. **251**, 237–258 (2000).

[43]T. Ogitsu, Y. Ping, A. Correa, B.-i. Cho, P. Heimann, E. Schwegler, J. Cao, and G. W. Collins, "Ballistic electron transport in non-equilibrium warm dense gold," High Energy Density Phys. **8**, 303–306 (2012).

[44]Yu. V. Petrov, K. P. Migdal, N. A. Inogamov, and V. V. Zhakhovsky, "Two-temperature equation of state for aluminum and gold with electrons excited by an ultrashort laser pulse," Appl. Phys. B **119**, 401–411 (2015).

[45]Y. V. Petrov, N. A. Inogamov, and K. P. Migdal, "Two-temperature heat conductivity of gold," in PIERS Proceedings, Prague, Czech Republic, 2015.

[46]T. Schneider and E. Stoll, "Molecular-dynamics study of a three-dimensional one-component model for distortive phase transitions," Phys. Rev. B **17**, 1302 (1978).

[47]P. Mabey, S. Richardson, T. G. White, L. B. Fletcher, S. H. Glenzer, N. J. Hartley, J. Vorberger, D. O. Gericke, and G. Gregori, "A strong diffusive ion mode in dense ionized matter predicted by Langevin dynamics," Nat. Commun. **8**, 14125 (2017).

[48]A. Medved, R. Davis, and P. A. Vasquez, "Understanding fluid dynamics from Langevin and Fokker–Planck equations," Fluids **5**, 40 (2020).

[49]G. E. Norman, S. V. Starikov, and V. V. Stegailov, "Atomistic simulation of laser ablation of gold: Effect of pressure relaxation," J. Exp. Theor. Phys. **114**, 792–800 (2012).

[50]E. A. Brandes and G. B. Brook, *Smithells Metals Reference Book*, 7th ed. (Butterworth-Heinemann, London, England, 1998).

[51]Y. S. Touloukian, R. K. Kirby, R. E. Taylor, and P. D. Desai, *Thermal Expansion: Metallic Elements and Alloys* (Plenum, New York, 1975).
[52]F. C. Campbell, *Elements of Metallurgy and Engineering Alloys* (ASM World Headquarters: ASM International, 2008).
[53]E. A. Brandes, *Smithell's Metal Reference Book* (Butterworths, London, England, 1983).
[54]V. Syneček, H. Chessin, and M. Simerska, "The temperature dependence of lattice vibrations in gold from X-ray diffraction measurements," Acta Crystallogr., Sect. A: Found. Adv. **A26**, 108–113 (1970).
[55]B. E. Warren, *X-Ray Diffraction* (Dover Publications, Mineola, NY, 1990).
[56]S. H. Glenzer and R. Redmer, "X-ray Thomson scattering in high energy density plasmas," Rev. Mod. Phys. **81**, 1625 (2009).
[57]T. G. White, P. Mabey, D. O. Gericke, N. J. Hartley, H. W. Doyle, D. McGonegle, D. S. Rackstraw, A. Higginbotham, and G. Gregori, "Electron-phonon equilibration in laser-heated gold films," Phys. Rev. B **90**, 014305 (2014).
[58]V. V. Stegailov and P. A. Zhilyaev, "Warm dense gold: Effective ion–ion interaction and ionisation," Mol. Phys. **114**, 509–518 (2016).
[59]J. Li, J. Zhou, T. Ogitsu, Y. Ping, W. D. Ware, and J. Cao, "Probing the warm dense copper nano-foil with ultrafast electron shadow imaging and deflectometry," High Energy Density Phys. **8**, 298–302 (2012).
[60]D. M. Riffe, X. Y. Wang, M. C. Downer, D. L. Fisher, T. Tajima, J. L. Erskine, and R. M. More, "Femtosecond thermionic emission from metals in the space-charge-limited regime," J. Opt. Soc. Am. B **10**, 1424–1435 (1993).
[61]Y. Ping, A. A. Correa, T. Ogitsu, E. Draeger, E. Schwegler, T. Ao, K. Widmann, D. F. Price, E. Lee, H. Tam, P. T. Springer, D. Hanson, I. Koslow, D. Prendergast, G. Collins, and A. Ng, "Warm dense matter created by isochoric laser heating," High Energy Density Phys. **6**, 246–257 (2010).
[62]M. Vos, R. P. McEachran, E. Weigold, and R. A. Bonham, "Elastic electron scattering cross sections at high momentum transfer," Nucl. Instrum. Methods Phys. Res., Sect. B **300**, 62–67 (2013).
[63]P. J. Brown, A. G. Fox, E. N. Maslen, M. A. O'Keefe, and B. T. M. Willis, "Intensity of diffracted intensities," in *International Tables for Crystallography Volume C* (Wiley, 2006), pp. 554–595.
[64]L. Reimer and H. Kohl, *Transmission Electron Microscopy: Physics of Image Formation* (Springer US, Boston, MA, 2008).
[65]R. F. Egerton, *Electron Energy-Loss Spectroscopy in the Electron Microscope* (Springer US, Boston, MA, 2014).
[66]T. Ida, M. Ando, and H. Toraya, "Extended pseudo-Voigt function for approximating the Voigt profile," J. Appl. Crystallogr. **33**, 1311–1316 (2000).
[67]Z. Lin and L. V. Zhigilei, "Time-resolved diffraction profiles and atomic dynamics in short-pulse laser-induced structural transformations: Molecular dynamics study," Phys. Rev. B **73**, 184113 (2006).
[68]X. W. Zhou, H. N. G. Wadley, R. A. Johnson, D. J. Larson, N. Tabat, A. Cerezo, A. K. Petford-Long, G. D. W. Smith, P. H. Clifton, R. L. Martens, and T. F. Kelly, "Atomic scale structure of sputtered metal multilayers," Acta Mater. **49**, 4005–4015 (2001).
[69]A. Stukowski, "Visualization and analysis of atomistic simulation data with OVITO–the open visualization tool," Modell. Simul. Mater. Sci. Eng. **18**, 015012 (2009).
[70]P. M. Larsen, S. Schmidt, and J. Schiøtz, "Robust structural identification via polyhedral template matching," Modell. Simul. Mater. Sci. Eng. **24**, 055007 (2016).
[71]Z. Lin, E. Leveugle, E. M. Bringa, and L. V. Zhigilei, "Molecular dynamics simulation of laser melting of nanocrystalline Au," J. Phys. Chem. C **114**, 5686–5699 (2010).